Journal of Applied Mathematics and Physics, 2025, 13(7), 2183-2198
https://www.scirp.org/journal/jamp
ISSN Online: 2327-4379
ISSN Print: 2327-4352

Efficiency Analysis of Terahertz Radiation Produced under Different Pumping Conditions of Two Femtosecond Laser Pulses

Abdelrahman I. Mahdy, Hoda A. Eltayeb

Plasma and Nuclear Fusion Department of Nuclear Research Centre, Egyptian Atomic Energy Authority, Cairo, Egypt
Email: aimahdy@yahoo.com

How to cite this paper: Mahdy, A.I. and Eltayeb, H.A. (2025) Efficiency Analysis of Terahertz Radiation Produced under Different Pumping Conditions of Two Femtosecond Laser Pulses. *Journal of Applied Mathematics and Physics*, **13**, 2183-2198.
https://doi.org/10.4236/jamp.2025.137124

Received: June 3, 2025
Accepted: July 1, 2025
Published: July 4, 2025

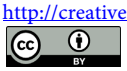

Abstract

We analyzed the efficiency of a terahertz radiation produced at different pumping conditions of a first harmonic (ω_0) Gaussian beam coupled with a second harmonic ($2\omega_0$) Laguerre-Gaussian vortex beam. In particular, we investigated the spatial-temporal properties of an induced THz vortex beam under an equal and unequal beams amplitudes filamentation conditions, and in different input intensity regions for each condition. In this respect, for every single filamentation condition, we numerically simulated the transverse intensity distribution and the phase-azimuthal angle modulation of the produced THz vortex beam in each given intensity region. Numerical results have justified that the generated THz vortex beam-shape is mainly the filamentation condition dependence, meanwhile the spatial-temporal properties of the induced beam are constrained to the input intensity region. On the whole, regardless of the filamentation condition, in the high-input intensity region more efficient largely anisotropic THz vortex beam with more refinement intensity and highly orbital angular momentum acceleration is demonstrated.

Keywords

High-Order FDTD, Maxwells Equations Solver, Terahertz Radiation Production, Filamentation of Femtosecond Laser, Kerr Nonlinearity

1. Introduction

The terahertz (THz) vortex beam is a light beam with a spiral wave front [1]. Because of its distinctive ability to carry an Orbital Angular Momentum (OAM) that is attributed to the correlated spatial phase distribution [2], the vortex THz beam is running in various real-life applications, ranging from the THz wireless com-

munication [3] to the detection of the astrophysical images [4], in addition to the super-resolution imaging [5], control the chirality of twisted metal nanostructures [6], and the electron bunch acceleration [7]. Basically, the production of THz vortex beams is maintained by two main mechanisms which are: 1) the wavefront modulation device mechanism; in which the vortex phase plates [8] and the THz hologram technology [9] [10] method are applied, and 2) the direct excitation of the THz vortex helicity mechanism; where the optical rectification (OR) [11], the difference frequency generation (DFG) [12] [13], and the spatially periodically and non-periodically modulation plasma [14] [15] method are employed. Among these mentioned methods, peculiar attention has been given to the spatially non-periodically modulation plasma method for its advantage to achieve a high intensity and broadband regular THz field behind the threshold damage of bulk materials [15]-[17].

In the non-periodically modulated plasma method, by the filamentation of a fundamental femtosecond beam (ω_0) and its second harmonic ($2\omega_0$) in air plasma an ultra-broad band THz angularly accelerated vortex beam is induced [18]. The THz beam production by this filamentation is govern by two models, namely the Fourth-Wave Mixing (FWM) [19] model; where the mixing process $\omega_0+\omega_0-2\omega_0\to\omega_{THz}$ or $-(\omega_0+\omega_0)+2\omega_0\to\omega_{THz}$ occurs, and the Photocurrent (PC) model [20]; in which by an asymmetric coupling between the two fs beams an oscillating optical current J is generated to emit a terahertz radiation. Based on the FWM and PC model, extensive researches have been conducted to study the production of the THz vortex beam at different pumping conditions of the two input fs beams. The central purpose of these researches is to examine the properties of the produced THz vortex radiation in order to underline the optimum input beams conditions for an efficient THz vortex beam production. At first, by adjusting the relative phase between two-color vortex laser beams [21], a controllable THz necklace-shaped vortex beam is demonstrated. Afterwards, using few cycle input vortex beams, various MIR-infrared vortex beams are generated [22], as at the low-input-frequency a MIR vortex beam with a simple π stepwise phase invariance with the azimuthal angle (θ) is induced, where at the high-input frequency an anisotropic MIR vortex beam that carrying OAM with nonlinearly invariance phase profile is produced. Then after, with a first harmonic Gaussian (ω_0) and a second harmonic Laguerre-Gaussian beam ($2\omega_0$) that is carrying a vortex topical charge ℓ with an intensity modulation feature along the azimuthal angle [23], a unique THz vortex beam structure is formed.

In advanced investigations, by tunning the chirping parameters of two few-cycle input fs beams in different input intensity regions [24], different vortex beam structures with diverse properties are established, for instance in low-input intensities where the Kerr effect (FWM) dominates over the plasma effect (PC) a THz vortex beam of uniform patterns with a constant angular velocity is formed, in medium-input intensities where the Kerr and Plasma effects are comparable an Angular Accelerated Vortex Beams (AAVBs) with linear phase-azimuthal angle

dependence is generated, and in high-input intensities where the plasma effect is dominated an AAVBs with strongly nonlinear azimuthal angle dependence on the relative phase profile is induced. Moreover, by the combination of a fundamental Laguerre-Gaussian fs vortex beam (FH) with a second harmonic Gaussian beam (SH) at variable relative amplitudes and conjugated topological [25] (TC) $\ell = \pm 2$, mm-scale length necklace THz beam with stepwise phase profile is generated, where at large scale of this combination both of AAVBs with linear and nonlinear phase profile can be obtained. In this article, we analyze the efficiency of produced THz vortex beams at different pumping conditions of two fs laser pulses, these conditions are the equal and unequal two fs beams amplitudes filamentation and the different input intensity regions for each filamentation case. The essential objective of this analysis is to determine the optimum pumping conditions for an efficient THz vortex beam production. In section 2, we present the physical model employed to conduct this study by listing its basic equations and explaining its physical assumptions. In section 3, we present for each of the equal and unequal beams amplitudes filamentation case, simulation results for the transverse intensity distributions and the relative-azimuthal angle relation of an induced THz vortex beam in three different input intensity regions.

2. The Physical Mode

In our efficiency analysis for the THz vortex beam induced under different pumping conditions of two input fs beams, the fundamental beam (FH) is a Gaussian (nonvortex) beam with wavelength $\lambda = 800$ nm (ω_0) and the second harmonic beam (SH) is a Laguerre-Gaussian vortex beam with $\lambda = 400$ nm ($2\omega_0$). The initial scalar combined field of the conventional vortex of these beams is given by

$$E(r,\theta,t) = \sum_{i}^{2} A_i(r) U_i(t) \mathrm{e}^{i\ell_i\theta}. \tag{1}$$

where $A(r)$ is the spatial part,

$$A_1(r) = A_2(r) = A(r) \to A(x,y),$$

and $U(t)$ is the temporal part,

$$U(t) = a\mathrm{e}^{-\left[2\ln(2)\frac{t^2}{\tau_1^2}\right]}\cos(\omega_0 t) + b\mathrm{e}^{-\left[2\ln(2)\frac{t^2}{\tau_2^2}\right]}\cos(2\omega_0 t + \Delta\phi),$$

where a,b are the initial real amplitudes, τ_1,τ_2 are the initial pulse durations of the FH and SH beams, respectively, ω_0 is the fundamental frequency, $\Delta\phi$ is the relative phase between the FH and SH.

$\mathrm{e}^{i\ell\theta}$ is the topological part,

$$\mathrm{e}^{i\ell\theta} = \mathrm{e}^{i(\ell_1\theta)} + \mathrm{e}^{i(\ell_2\theta)},$$

where θ is the azimuthal angle and ℓ is the topological charge (TC).

In our numerical calculations [26], both the FH and SH beam have the same initial pulse duration $\tau_1 = \tau_2 = \tau_0 = 5$ fs, and for the nonvortex FH beam $\ell_1 = 0$ and for the SH vortex beam $\ell_2 = \ell = 1$. Thus, the initial scalar combined field can

be finally written as:

$$E(r,\theta,t)=A(r)\left[a\cos(\omega_0 t)+b\cos(2\omega_0 t+\Delta\phi)\right]\mathrm{e}^{-\left[2\ln(2)\frac{t^2}{\tau_0^2}\right]}\mathrm{e}^{i\ell\theta}. \tag{2}$$

Our air plasma is the Nitrogen gas N_2 at initial density $n_e=2.7\times10^{19}cm^{-3}$ that is Tunneling Ionizing (TI) by the input femtosecond beams. Herein, the ionization rate is the standard ADK formula [27].

$$\omega(r,\theta,t)=4\omega_a\frac{\left(U_{N_2}/U_H\right)^{2.5}}{A(r,\theta,t)}\mathrm{e}^{-\left[\frac{2\left(U_{N_2}/U_H\right)^{1.5}}{3\quad A(r,\theta,t)}\right]} \tag{3}$$

$\omega_{at}=mq^2/\left(4\pi\epsilon_0^2\right)\hbar^3=4.134\times10^{16}\ \mathrm{s}^{-1}$ is the atomic frequency, U_{N_2},U_H are the ionization potential of Hydrogen and Nitrogen molecules, respectively. $A(r,\theta,t)=|E_L|/|E_{at}|$ is the optical field strength in atomic unit, where E_L is the electric field of the applied fs beams and $E_{at}=m^2q^5/\left(4\pi\epsilon_0^3\right)\hbar^4=5.14\times10^9\ \mathrm{V/cm}$ is the atomic unit of the electric field.

3. Simulation Results

The filamentation of two fs beams in air plasma is the principle mechanism of our terahertz radiation production [18]. As known, this filamentation is demonstrated when the self-focusing by the Kerr nonlinearly and the defocussing by the nonlinear plasma ionization effects is balance. Essentially, this balance is achieved at the namely known the clamping intensity [28], the clamping intensity (I_c) is the peak intensity that is constricted inside the plasma filament when the length of the filament starts to increase. The clamping intensity value is the propagation conditions and the plasma structures dependence, for example: in case of an applied polarized beams, $I_c=5\times10^{13}\ \mathrm{W/cm^2}$ is the simulated value [28] at $\lambda=800\ \mathrm{nm}$, while $I_c=15\ \mathrm{TW/cm^2}$ is the proper value at $n_e=2.2\times10^{15}\ \mathrm{cm^{-3}}$ under the influences of the freeman resonance [29]. In a similar to our filamentation condition and air plasma structure, the $I=30\sim80\ \mathrm{TW/cm^2}$ is input intensity period [30] where the clamping intensity is effective and the THz radiation is generated. In a correlation between this effective clamping intensity period and the Kerr and plasma nonlinearity effects, in the THz vortex beams production researches this period is classified into: 1) the low input intensity region ($I<28\ \mathrm{TW/cm^2}$) where the input intensity is less than the clamping intensity and the Kerr nonlinearity effects is predominated, 2) the medium-input intensity region wherein the input intensity nearly equal the clamping intensity ($I=28\sim53\ \mathrm{TW/cm^2}$) and the Kerr and plasma nonlinearity effects are comparative and competitive, and 3) the high-input intensity region ($I>53\ \mathrm{TW/cm^2}$) at which the input intensity larger than the clamping intensity and the plasma nonlinearity is the dominated effects. In this research, we are crucially interested to conduct an elaborated analysis for the spatial and temporal properties of the produced THz vortex beams for the equal and unequal input beams amplitudes filamentation, in each of these listed input intensity regions.

3.1. The THz Vortex Beams Production by Two fs Beams of Equal Amplitudes

In Figure 1(a) we present the transverse intensity distribution of a THz vortex beam induced by two fs beams with equal amplitudes in the low-input intensity region. As shown in this distribution, a doughnut shape intensity patterns (ring-shaped) with zero intensity in the center is demonstrated. As clearly seen in this demonstration, the intensity patterns are spatiality symmetrically distributed and shaped out of a main ring that is largely spreed over the transverse space and preserves the major non-distortion intensity of the induced THz vortex beam. In addition to this, the main ring is surrounding with few numbers of rings with much larger width and lower intensity. In fact, the ring-shaped THz vortex beam is previously observed in a number of studies, in one of this study [24] that has been conducted at the similar pumping conditions of our study, ring patterns with zero central intensity is also formed, while in another study [25] where the FH beam is LG and the SH is Gaussian, ring patterns with non-zero intensity center is produced, the SH ($2\omega_0$) Gaussian input beam is the responsible of this non-zero intensity center as it is explained in this study.

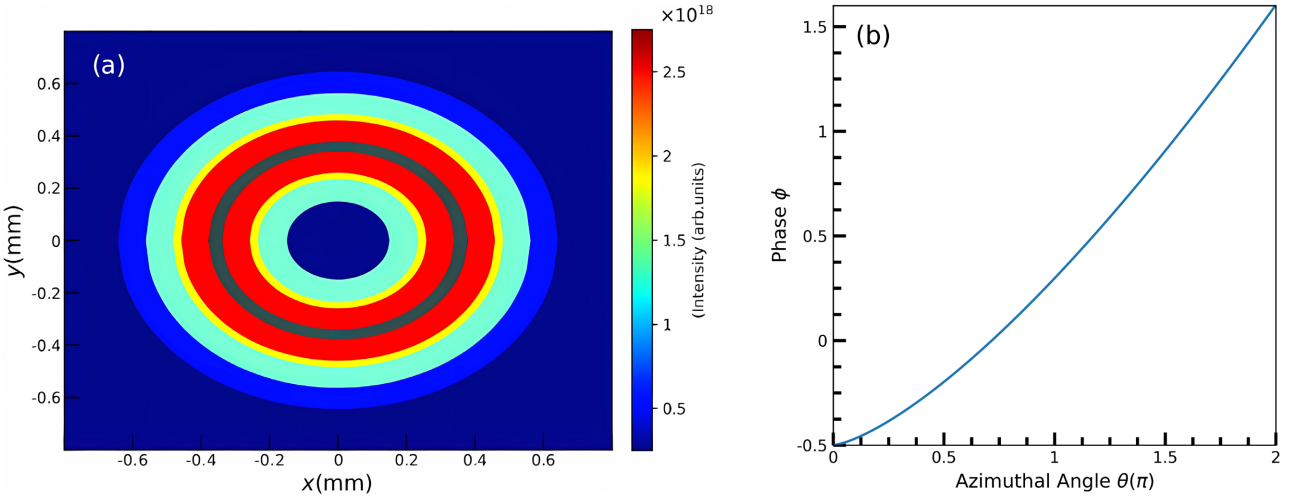

Figure 1. The transverse intensity distribution (left) and the phase azimuthal angle relation (right) of a THz vortex beam induced by the filamentation of two fs beams with equal amplitudes in the low-input intensity region.

To analyze the temporal properties of the induced ring-shaped THz vortex beam, we display the phase ϕ and the azimuthal angle θ relation of this shape in Figure 1(b). As seen in this figure, the ϕ is linearly evolving with θ, the linear $\phi-\theta$ relation indicates that $\partial\phi/\partial\theta \approx$ constant and the phase-azimuthal angle is non-modulated dependence which implies that the demonstrated ring-shaped patterns displayed in Figure 1(a) has no Orbital Angular Momentum (OAM). It is important to bear in mind that, although the Kerr nonlinearity is predominated in the low-input intensity region, the refractive index variation $\Delta n_{Kerr} = n_2 I_{pk}$ value due to this nonlinearity; where $n_2 = 2\times10^{-19}\,\mathrm{cm}^2/\mathrm{W}$ is the nonlinear refractive index in air and I_{pk} is peak intensity, is not adequate to per-

suade $\Delta\phi$ variation and modulate the $\phi-\theta$ dependence in this region, thus ϕ is linearly ($\phi=\ell\theta$) evolving with θ as displayed in **Figure 1(b)**, accordingly spatiality symmetric non-rotating ring-shaped THz vortex beam with the doughnut intensity patterns is demonstrated in **Figure 1(a)**.

In **Figure 2(a)**, we re-present the transverse intensity distribution of a THz beam induced by two equal fs beams amplitudes in the medium-input intensity region, a distinct development in the induced THz vortex beam structure is exploited in this figure. As illustrated in this distribution and in comparison with **Figure 1(a)**, the ring-shaped is modified into two-petals-shaped intensity patterns, the modified patterns are spatiality asymmetrically distributed over a circular ring that has approximately the same radius of the main ring displayed in **Figure 1(a)**, as well as, each petal preserves a higher intensity that is confined in a narrower transverse space. To interpret this modified THz vortex beam structure, it is necessary to clarify that in the medium-input intensity region the Kerr and plasma nonlinearity effects are competitive and comparative, other than that each Δn_{kerr} value due to the Kerr nonlinearity and $\Delta n_{plas}=-VN_e$ value due to the plasma nonlinearity; where $V=(4/9)e^2/\epsilon_0 m_e\omega_0^2$ is the effective volume of the plasma [31], is high enough [24], on that account the impacts of the total refractive variation $\Delta n=\Delta n_{Kerr}+\Delta n_{plas}$ on the phase variation [31] ($\Delta\phi=\Delta n\omega_0 L_{plas}/c$) are highly considered. Within this interpretation and because of the direct dependence of the generated THz beam amplitude $E_{THz}\propto\cos(\Delta\phi)$ on the resulted phase variation $\Delta\phi$, the preliminary impact of this dependence is the developed spatiality asymmetric two-petals-shaped intensity patterns structure formed in **Figure 2(a)**.

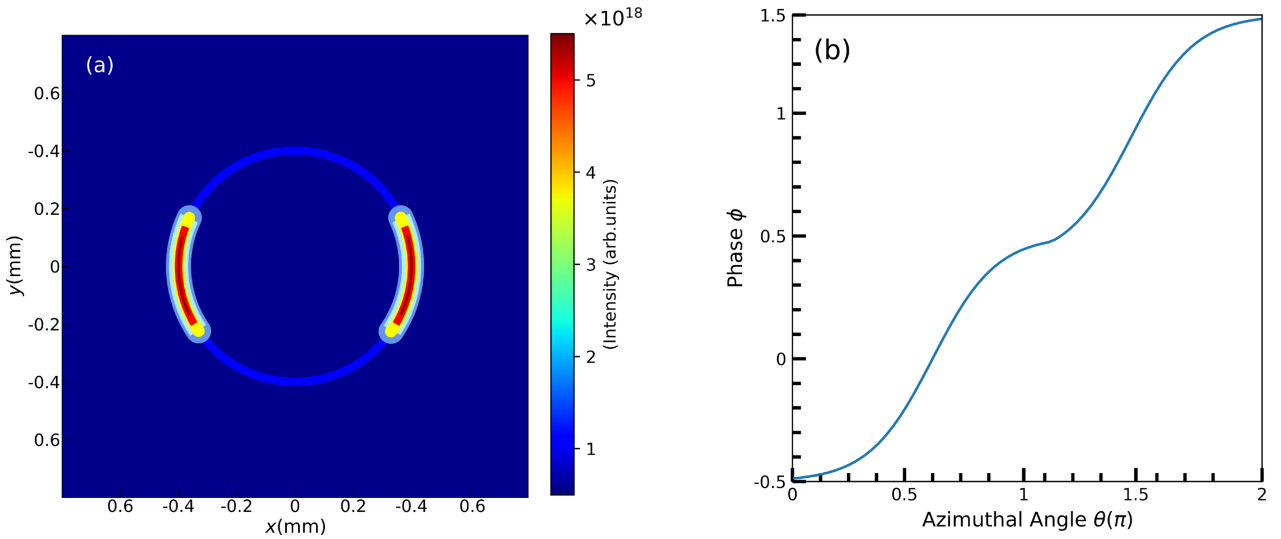

Figure 2. The transverse intensity distribution (left) and the phase azimuthal angle relation (right) of a THz vortex beam induced by the filamentation of two fs beams with equal amplitudes in the medium-input intensity region.

The additional impact of the resulted $\Delta\phi$ variation on the temporal properties of the induced two-petals-shaped THz vortex beam is analyzed in **Figure 2(b)** where the phase-azimuthal angle relation of a THz beam induced by two equal fs

beams amplitudes in the medium-input intensity region is display. As noted in this figure, the phase ϕ is nonlinearly evolving with θ, i.e., $\partial\phi/\partial\theta \neq$ constant, within this context, the phase is azimuthally modulated which implies that the two-petal patterns exposed in **Figure 1(a)** has an Orbital Angular Momentum (OAM). Thereupon, the direct impacts of the phase variation $\Delta\phi$ resulted by the total refractive variation Δn due to the Kerr and plasma nonlinearity effects in the medium-input intensity region is the developed rotated anisotropic two-petals-shaped THz vortex beam demonstrated in **Figure 2(a)**.

It has been recognized from the above results that depending on the input intensity region, the phase variation $\Delta\phi$ resulted due to the influential effects of the Kerr and plasma nonlinearity and its relation with the azimuthal angle θ is the origin of developing the THz vortex beam structure and modifying its spatial-temporal properties. In the high-input intensity region, because $\Delta n_{plas} \gg \Delta n_{Kerr}$ [24], the kerr and plasma nonlinearities effects are no-more comparative and the plasma nonlinearity is the dominated effects. Be noted that, the plasma nonlinearity has a distinguished characteristic which is the tunneling ionization is achieving at the peak intensity of the input beams, upon that the ultimate energy is delivered to the air plasma at that moment. The direct impact of this feature is clearly observed in **Figure 3(a)**, as noted the intensity patterns are to a great extent spatially asymmetrically distributed over a narrower ring, moreover the intensity of these patterns is even more reinforced where its maximum values are confined in narrower spatial space.

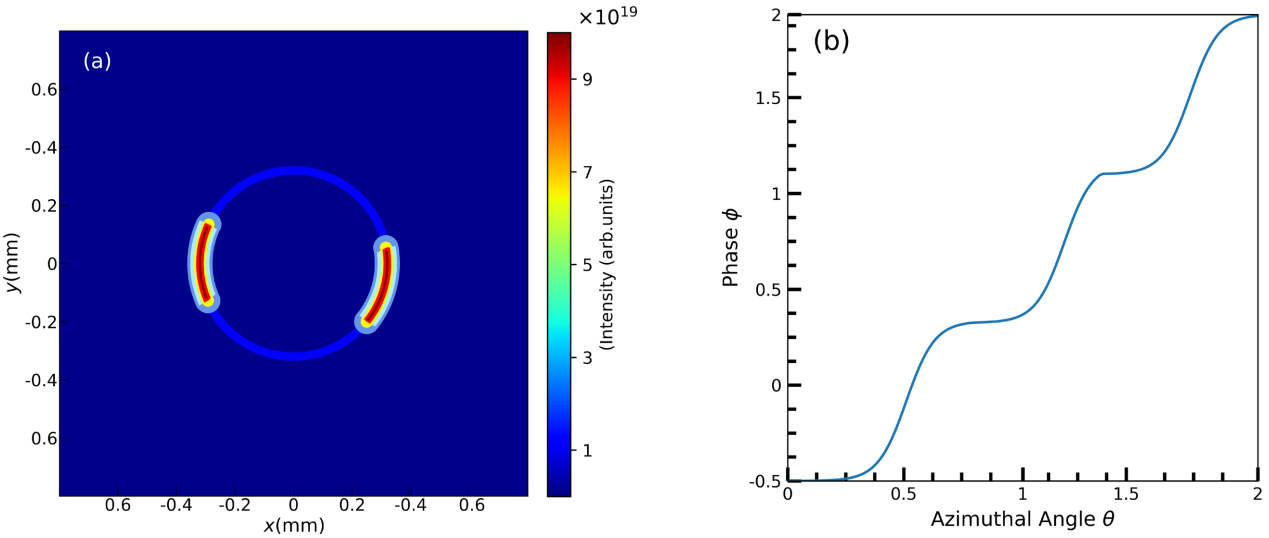

Figure 3. The transverse intensity distribution (left) and the phase azimuthal angle relation (right) of a THz vortex beam induced by the filamentation of two fs beams with equal amplitudes in the high-input intensity region.

To explore the impact of the plasma nonlinearly domination in the high-input region and its peculiar feature on the temporal properties of the induced two-petals-shaped, in **Figure 3(b)** the phase as function of the azimuthal angle of a THz vortex beam induced by two equal amplitudes fs beam in the high-input in-

tensity region is shown. As clear in this figure and in comparison with Figure 2(b), the phase ϕ is strongly nonlinearly evolving with θ, this rigorous nonlinearity leads to the highly modulated $\phi-\theta$ dependence which escalates the OAM acceleration. Thus, in the high-input intensity region, more efficient two-petal-shaped THz vortex beam with more enhancement intensity and accelerated rotation is established as shown in Figure 3(a).

3.2. The THz Vortex Beams Production by Two fs Beams of Unequal Amplitudes

The filamentaion of two unequal fs beams amplitudes in air plasma is a nonlinear dynamics of a crucial importance in the long-range fs beams propagating [32]. Numerous processes, such as spontaneous symmetry breaking [33] and the cross-correlation technique [34] are taking place during this filamentation, even so, the energy exchange between the two unequal fs beams amplitudes is the most vital among these processes for its boarded applications in supercontinum generation [35], lightning and discharge triggering [36], remote sensing [37], and THZ radiation production [38]. The energy exchange is a promising nonlinear process in controlling the multi fs beams propagation, in any case, the exchange rate and direction depend on the relative time delay, the initial chirps, the input intensities, the intersection angle, and the relative polarization of the two fs beams. The plasma mediated forward Simulated Raman Scattering (SRS) [39], the Traveling Plasma Grating (TPG) [40]-[42], and the Two Beams Coupling (TBC) are the primitive mechanisms to govern the energy exchange. In our study, the TBC is the employed mechanism since it is appropriate whenever a frequency difference between the pumping beams is applied. In this section, we analyze the efficiency $\eta_{THz}=\int_0^{THz}\left|E(\omega)\right|^2 \mathrm{d}\omega \Big/ \int_0^t \left|E(r,\theta,t)\right|^2 \mathrm{d}t$ of the produced THz vortex beams induced by the filamentaion of two unequal fs beams amplitudes, the role of emerged energy exchange process on the efficiency and the spatial-temporal properties of the produced THz vortex beam in the three input intensity regions will be investigated.

In Figure 4(a), we present the transverse intensity distribution of a THz beam induced by the superposition of two fs beams with unequal amplitudes in the low-input intensity region. As depicted in this figure, a necklace-shaped THz vortex beam with four identical petals is demonstrated. It is noteworthy that in the THz vortex beams researches, the petal-like-shaped and ring-shaped are the predominated and the most excepted structures, even so, these structures have different and separated intensity patterns distribution. In contrast, the petal-like-shaped patterns are centrally located, while the ring-shape patterns that have lower intensity are spreading over a larger area. Due to the overlapping of these two structures [43] in the presence of the energy exchange in the low-input intensity region, spatiality symmetric necklace-shaped THz vortex beam with four identical petals is demonstrated as seen in Figure 4(a).

The necklace-shaped THz vortex beam is an interesting light beam structure

that has a growing applications ranging from cold atom manipulation to optically driven micromachines [44] [45]. Overall, the necklace THz vortex beam with and without OAM has been theoretically and experimentally predicated [46] [47], on that account to examine the temporal properties of our induced necklace THz vortex beam, the phase and the azimuthal angle relation for the two fs beam with unequal amplitudes in the low-intensity region is displayed in **Figure 4(b)**. As noted in this figure, a π -stepwise phase profile is observed for each of the two lobes that are separated at $\theta = \pi$. The observed profile marks that this necklace-shaped beam has no OAM, in addition the abruptly change of this profile at $\theta = \pi$ implies the reverse polarity $(\pm ve)$ of the induced THz beam phase for each lobe. The non-rotating spatially symmetric intensity patterns is anticipated in the low-input intensity region, as in this region, although the Kerr effect is prevailed, Δn_{kerr} value is small to develop $\Delta\phi$ variation, furthermore the energy exchange magnitude and rate is not sufficient enough to produce a phase variation and then an azimuthal angle modulation. As a result, the non-accelerated spatially symmetric necklace-shaped THz vortex beam with four identical petals that have equal maximum intensity is demonstrated in **Figure 4(a)**.

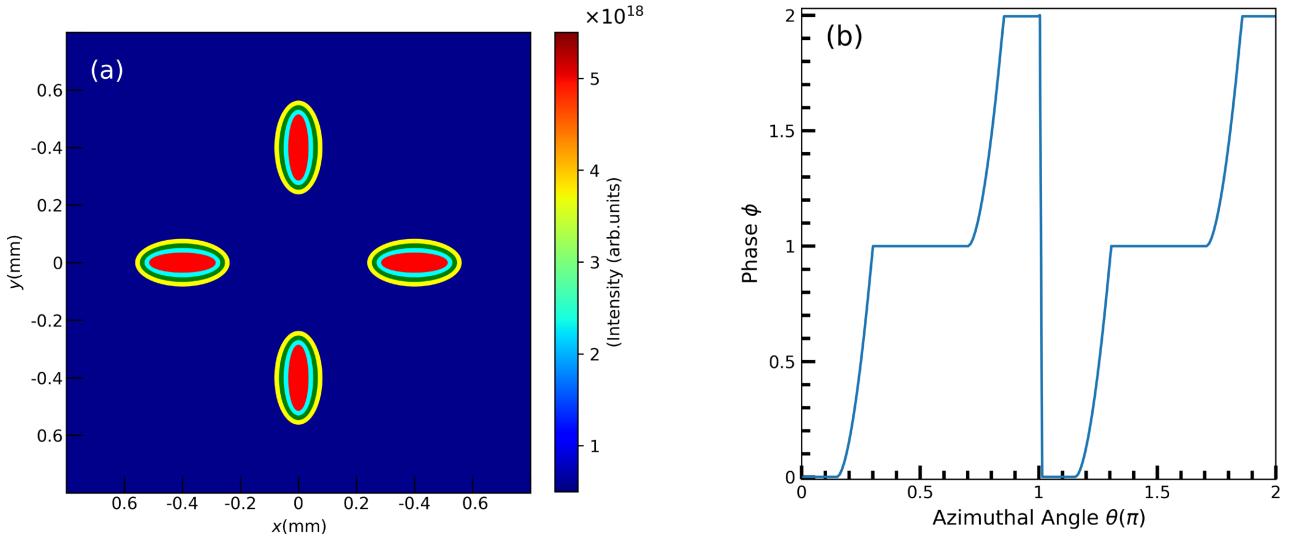

Figure 4. The transverse intensity distribution (left) and the phase azimuthal angle relation (right) of a THz vortex beam induced by the filamentation of two fs beams with unequal amplitudes in the low-input intensity region.

In **Figure 5(a)**, we re-present the transverse intensity distribution of a THz vortex beam generated due to the superposition of two fs beams with unequal amplitudes in the medium-input intensity region. Although a necklace-shaped THz vortex beam with four-petals intensity patterns is remained in this figure, in comparison with **Figure 4(a)**, a notable reformation in respect to the spatial properties of these patterns is emerged. As clear in **Figure 5(a)**, the four-petals are spatially asymmetrically distributed over narrower ring, where each petal is randomly displaced and preserves more refinement maximum intensity that is confined in a narrower space. As explained before, the $\Delta\phi$ resulted by to the total refractive

variation Δn due the kerr and plasma nonlinearity in the medium-input intensity region is origin of this spatiality asymmetric reshaping, meanwhile the presence of the energy exchange, additional nonlinear effects should be regarded which is the Cross Phase Modulation [48] (XPM). The XPM is a nonlinear temporal-spatial modulation that is established by the overlapping between the two unequal fs beams amplitudes, during this overlapping the phase of one beam modulates the counterpart one as these beams propagating through the nonlinear medium. In principle, the XPM induces arbitrarily velocity, peak beam intensity, and relative phase modulation $\Delta\phi^{XPM}$ through the refractive index variation $\Delta n_{XPM} = \delta n_2^{XPM} I_{pro}$. As matter of fact, XPM that is the propagating beam intensity dependence I_{pro}, therefore it is considered as part of kerr nonlinearity. For this reason, in the present study the XPM nonlinearity is summed with the conventional Kerr nonlinearity effect, accordingly, the refractive index variation due to the kerr effects is updated by $\Delta n_{Kerr} = n_2 I_{pk} + \delta n_2^{XPM} I_{pro}$.

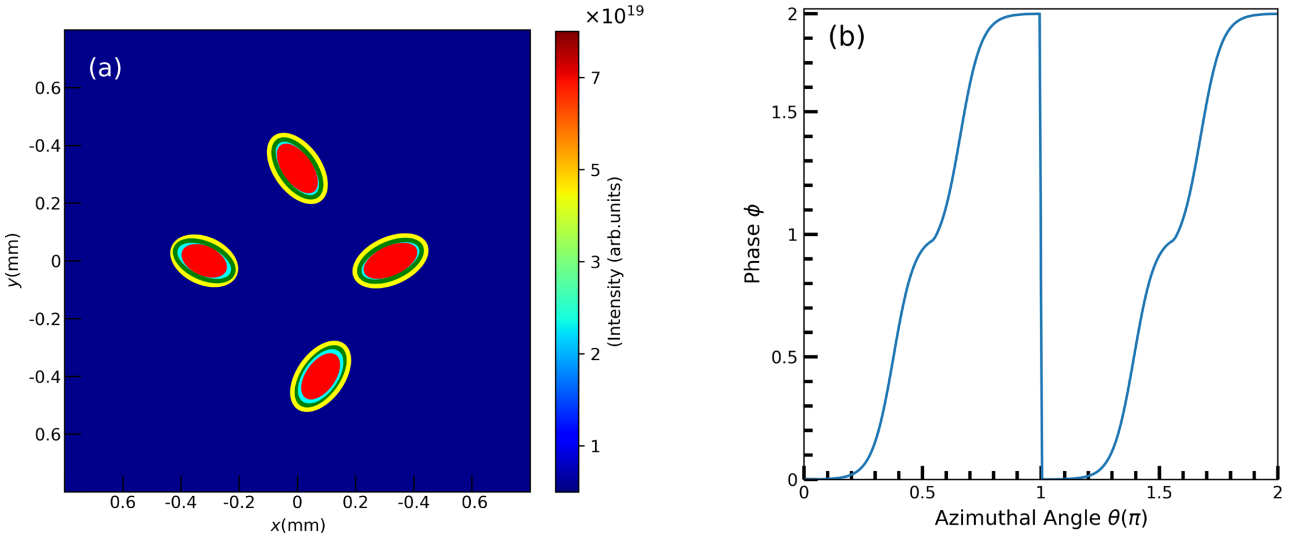

Figure 5. The transverse intensity distribution (left) and the phase azimuthal angle relation (right) of a THz vortex beam induced by the filamentation of two fs beams with unequal amplitudes in the medium-input intensity region.

After we have affirmed the spatial asymmetric properties of the induced necklace-shaped THz vortex beams in the medium-input intensity region, the temporal properties of this shape in this region should be examined as well. In **Figure 5(b)** we display phase-azimuthal angle relation of a THz beam induced due to the superposition of two fs beams with unequal amplitudes in the low-input intensity region. Although the phase profile is jumping up at the separated lobe point $\theta = \pi$, in this figure, per each lobe the ϕ is nonlinear evolving with θ, on that $\partial\phi/\partial\theta$ is not constant, and thus this induced reshaped has OAM. Thereby, the necklace-shape THz vortex beam formed in **Figure 5(a)** is spatially anisotropic and angularly momentum accelerating.

As we have previously explained, in the high-input intensity region the plasma nonlinearity is the dominated effect and the phase variation $\Delta\phi$ is mostly re-

sulted due to Δn_{plas}. For the two unequal beams amplitudes filamentation case, in the high-input intensity region, due to plasma nonlinearity domination and the presence of the energy exchange, the resulted $\Delta\phi$ has straightforward impact on the oscillation optical current $J = I\Delta\phi$ that consequently influences on the induced patterns intensity (I_z) through the intensity transport equation [49]

$$\partial I_z = \frac{1}{k}\nabla \cdot J, \tag{4}$$

where ∂I_z patterns intensity of the energy exchange during the propagation. To look into the consequences of the updated $\Delta\phi$ impact and influence on the spatial properties of the induced necklace-shaped THz vortex beam, we display in **Figure 6(a)** the transverse intensity distribution of an induced THz vortex beam by the superposition of two fs beams with unequal amplitudes in the high-input intensity region. In comparison with **Figure 5(a)**, the spatial properties of the induced necklace THz vortex beam is further developing, as represented, the four-petals of the remained necklace-shaped are highly spatially asymmetrically distributed over more narrower ring, beside each petal is largely randomly displaced and preserves extra refinement maximum intensity that is confined in more tight space.

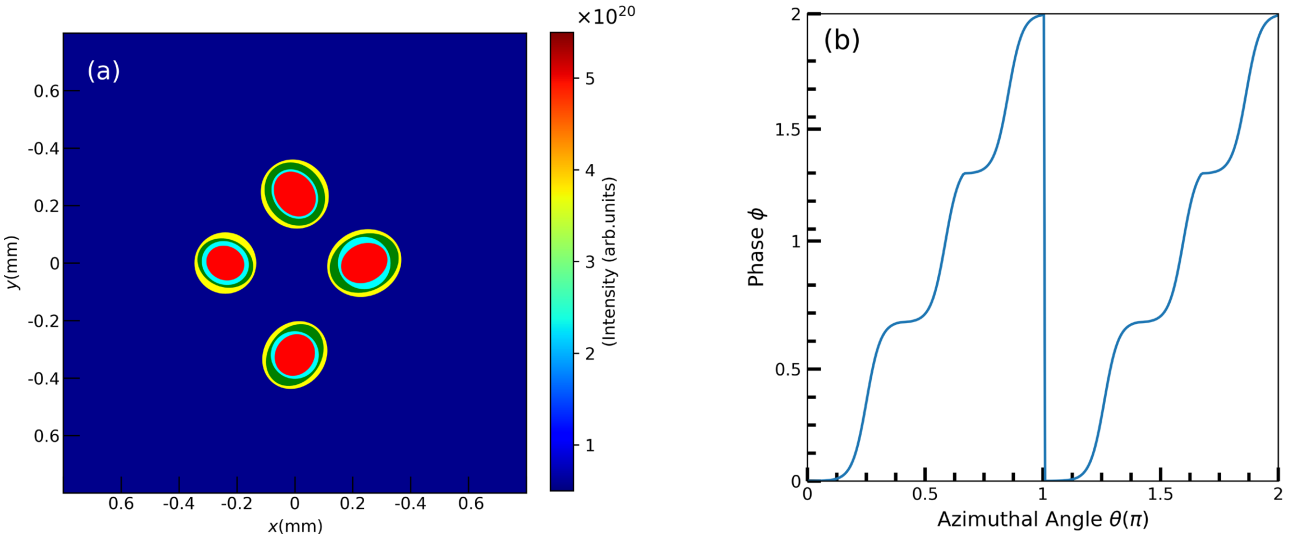

Figure 6. The transverse intensity distribution (left) and the phase azimuthal angle relation (right) of a THz vortex beam induced by the filamentation of two fs beams with unequal amplitudes in the high-input intensity region.

To follow up the impact and influence of the updated $\Delta\phi$ on the temporal properties on this induced beam, in **Figure 6(a)** we show phase-azimuthal angle relation of two fs beams with unequal amplitudes in the high-input intensity region. As illustrated in this figure and in a comparison with **Figure 5(a)**, per each lobe, the $\phi - \theta$ is more nonlinearly evolving, hence more efficient and highly accelerated THz vortex necklace-shaped THz vortex beam with largely anisotropic petals distribution that preserve more confined maximum intensity for each petal is demonstrated in **Figure 6(a)**.

4. Conclusion

We analyzed the spatial-temporal properties of THz vortex beams induced under an equal and unequal two fs beams amplitudes filamentation conditions, and in three different input intensity regions for each condition. Numerical simulations have revealed that in the equal beams amplitudes filamentation case, a spatiality symmetric non-rotated ring-shaped THz vortex beam is demonstrated in the low-input intensity region, while in the medium-input intensity region where the Kerr and plasma nonlinearity effects start to be influential, the ring-shaped THz vortex beam is modified into higher intensity anisotropic two-petals-shaped that is associated with OAM, meanwhile in the high-input intensity region where the plasma nonlinearly is the main key player, the properties of this modified anisotropic beam is more enhanced to preserve more higher intensity at more accelerated OAM. In the unequal beams amplitudes filamentation case and in the presence of the energy exchange between these amplitudes, in the low-input intensity region spatiality symmetric non-rotated necklace-shaped THz vortex beam with four identical petals is demonstrated, even though in the medium-input intensity region where the updated Kerr and plasma nonlinearity effects are comparatively influential, the necklace-shaped is remained but with spatiality anisotropic non identical four-petals-shaped at larger intensity and angular momentum acceleration, on the other hand in the high-input intensity region where the plasma nonlinearly is dominated, more refinement necklace-shaped THz vortex beam is formed at more confined and magnified intensity with an increasing angular momentum acceleration. Regardless of the filamentation condition and the demonstrated THz vortex beam shaped, in the high-input intensity region and due to the dominated plasma nonlinearity effects, more efficient THz vortex beam is produced.

Conflicts of Interest

The authors declare no conflicts of interest regarding the publication of this paper.

References

[1] Yao, A.M. and Padgett, M.J. (2011) Orbital Angular Momentum: Origins, Behavior and Applications. *Advances in Optics and Photonics*, **3**, 161-204. https://doi.org/10.1364/aop.3.000161

[2] Allen, L., Beijersbergen, M.W., Spreeuw, R.J.C. and Woerdman, J.P. (1992) Orbital Angular Momentum of Light and the Transformation of Laguerre-Gaussian Laser Modes. *Physical Review A*, **45**, 8185-8189. https://doi.org/10.1103/physreva.45.8185

[3] Malhotra, I., Jha, K.R. and Singh, G. (2018) Terahertz Antenna Technology for Imaging Applications: A Technical Review. *International Journal of Microwave and Wireless Technologies*, **10**, 271-290. https://doi.org/10.1017/s175907871800003x

[4] Harwit, M. (2003) Photon Orbital Angular Momentum in Astrophysics. *The Astrophysical Journal*, **597**, 1266-1270. https://doi.org/10.1086/378623

[5] Watanabe, T., Iketaki, Y., Omatsu, T., Yamamoto, K., Sakai, M. and Fujii, M. (2003) Two-Point-Separation in Super-Resolution Fluorescence Microscope Based on Up-

Conversion Fluorescence Depletion Technique. *Optics Express*, **11**, 3271-3276. https://doi.org/10.1364/oe.11.003271

[6] Toyoda, K., Miyamoto, K., Aoki, N., Morita, R. and Omatsu, T. (2012) Using Optical Vortex to Control the Chirality of Twisted Metal Nanostructures. *Nano Letters*, **12**, 3645-3649. https://doi.org/10.1021/nl301347j

[7] Zhang, D., Fallahi, A., Hemmer, M., Wu, X., Fakhari, M., Hua, Y., *et al.* (2018) Segmented Terahertz Electron Accelerator and Manipulator (Steam). *Nature Photonics*, **12**, 336-342. https://doi.org/10.1038/s41566-018-0138-z

[8] Schemmel, P., Maccalli, S., Pisano, G., Maffei, B. and Ng, M.W.R. (2014) Three-Dimensional Measurements of a Millimeter Wave Orbital Angular Momentum Vortex. *Optics Letters*, **39**, 626-629. https://doi.org/10.1364/ol.39.000626

[9] Ala-Laurinaho, J., Hirvonen, T., Piironen, P., Lehto, A., Tuovinen, J., Raisanen, A.V., *et al.* (2001) Measurement of the Odin Telescope at 119 GHz with a Hologram-Type CATR. *IEEE Transactions on Antennas and Propagation*, **49**, 1264-1270. https://doi.org/10.1109/8.947017

[10] Salo, J., Meltaus, J., Noponen, E., L$ouml$nnqvist, A., Koskinen, T., *et al.* (2002) Holograms for Shaping Radio-Wave Fields. *Journal of Optics A*: *Pure and Applied Optics*, **4**, S161-S167. https://doi.org/10.1088/1464-4258/4/5/365

[11] Dhaybi, A.A., Degert, J., Brasselet, E., Abraham, E. and Freysz, E. (2018) Terahertz Vortex Beam Generation by Infrared Vector Beam Rectification. *Journal of the Optical Society of America B*, **36**, 12-18. https://doi.org/10.1364/josab.36.000012

[12] Lin, Q., Zheng, S., Song, Q., Zeng, X., Cai, Y., Li, Y., *et al.* (2019) Generation of Terahertz Vortex Pulses without Any Need of Manipulation in the Terahertz Region. *Optics Letters*, **44**, 887-890. https://doi.org/10.1364/ol.44.000887

[13] Miyamoto, K., Sano, K., Miyakawa, T., Niinomi, H., Toyoda, K., Vallés, A., *et al.* (2019) Generation of High-Quality Terahertz OAM Mode Based on Soft-Aperture Difference Frequency Generation. *Optics Express*, **27**, 31840-31849. https://doi.org/10.1364/oe.27.031840

[14] Sobhani, H. and Dadar, E. (2019) Terahertz Vortex Generation Methods in Rippled and Vortex Plasmas. *Journal of the Optical Society of America A*, **36**, 1187-1196. https://doi.org/10.1364/josaa.36.001187

[15] Bai, Y., Song, L., Xu, R., Li, C., Liu, P., Zeng, Z., *et al.* (2012) Waveform-Controlled Terahertz Radiation from the Air Filament Produced by Few-Cycle Laser Pulses. *Physical Review Letters*, **108**, Article ID: 255004. https://doi.org/10.1103/physrevlett.108.255004

[16] Kreß, M., Löffler, T., Thomson, M.D., Dörner, R., Gimpel, H., Zrost, K., *et al.* (2006) Determination of the Carrier-Envelope Phase of Few-Cycle Laser Pulses with Terahertz-Emission Spectroscopy. *Nature Physics*, **2**, 327-331. https://doi.org/10.1038/nphys286

[17] Roskos, H.G., Thomson, M.D., Kreß, M. and Löffler, T. (2007) Broadband THz Emission from Gas Plasmas Induced by Femtosecond Optical Pulses: From Fundamentals to Applications. *Laser & Photonics Reviews*, **1**, 349-368. https://doi.org/10.1002/lpor.200710025

[18] Couairon, A. and Mysyrowicz, A. (2006) Femtosecond Filamentation in Air. In: Couairon, A. and Mysyrowicz, A., Eds., *Progress in Ultrafast Intense Laser Science Volume I*, Springer, 235-258. https://doi.org/10.1007/3-540-34422-5_13

[19] Cook, D.J. and Hochstrasser, R.M. (2000) Intense Terahertz Pulses by Four-Wave Rectification in Air. *Optics Letters*, **25**, 1210-1212.

https://doi.org/10.1364/ol.25.001210

[20] Kim, K. (2009) Generation of Coherent Terahertz Radiation in Ultrafast Laser-Gas Interactions. *Physics of Plasmas*, **16**, Article ID: 056706. https://doi.org/10.1063/1.3134422

[21] Wang, H., Bai, Y., Wu, E., Wang, Z., Liu, P. and Liu, C. (2018) Terahertz Necklace Beams Generated from Two-Color Vortex-Laser-Induced Air Plasma. *Physical Review A*, **98**, Article ID: 013857. https://doi.org/10.1103/physreva.98.013857

[22] Wang, H., Song, Q., Zheng, S., Lin, Q., Wu, E., Ai, Y., *et al.* (2019) Terahertz-Mid-infrared Anisotropic Vortex Beams Generation via Few-Cycle Vortex-Laser-Induced Air Plasma. *Journal of Optics*, **21**, Article ID: 095501. https://doi.org/10.1088/2040-8986/ab2d84

[23] Ivanov, M., Thiele, I., Bergé, L., Skupin, S., Buožius, D. and Vaičaitis, V. (2019) Intensity Modulated Terahertz Vortex Wave Generation in Air Plasma by Two-Color Femtosecond Laser Pulses. *Optics Letters*, **44**, 3889-3892. https://doi.org/10.1364/ol.44.003889

[24] Wang, H., Song, Q., Cai, Y., Lu, X., Lin, Q., Zeng, X., *et al.* (2022) Local OAM Manipulation of a Terahertz Wave from the Air Filament by Chirping the Few-Cycle Vortex Pump Laser. *Optics Express*, **30**, 9727-9744. https://doi.org/10.1364/oe.452414

[25] Wang, H., Shangguan, H., Song, Q., Cai, Y., Lin, Q., Lu, X., *et al.* (2021) Generation and Evolution of Different Terahertz Singular Beams from Long Gas-Plasma Filaments. *Optics Express*, **29**, 996-1010. https://doi.org/10.1364/oe.413483

[26] Mahdy, A. (2025) Two-step Asymmetric Perfectly Matched Layer Model for High-Order Spatial FDTD Solver of 2D Maxwell's Equations. *Journal of Applied Mathematics and Physics*, **13**, 553-566. https://doi.org/10.4236/jamp.2025.132030

[27] Ammosov, M.V., Delone, N.B. and Krainov, V.P. (1986) Tunnel Ionization of Complex Atoms and Atomic Ions in Electromagnetic Field. *SPIE Proceedings*, **664**, 1191-1194. https://doi.org/10.1117/12.938695

[28] Guo, H., Dong, X., Wang, T., Zhang, X., Chen, N., Yin, F., *et al.* (2021) Polarization Dependent Clamping Intensity Inside a Femtosecond Filament in Air. *Chinese Optics Letters*, **19**, Article ID: 103201. https://doi.org/10.3788/col202119.103201

[29] Hofmann, M. and Brée, C. (2015) Femtosecond Filamentation by Intensity Clamping at a Freeman Resonance. *Physical Review A*, **92**, Article ID: 013813. https://doi.org/10.1103/physreva.92.013813

[30] Wu, H., Meyer-ter-Vehn, J. and Sheng, Z. (2008) Phase-Sensitive Terahertz Emission from Gas Targets Irradiated by Few-Cycle Laser Pulses. *New Journal of Physics*, **10**, Article ID: 043001. https://doi.org/10.1088/1367-2630/10/4/043001

[31] Lin, Y., Nabekawa, Y. and Midorikawa, K. (2016) Conical Third-Harmonic Generation of Optical Vortex through Ultrashort Laser Filamentation in Air. *Optics Express*, **24**, 14857-14870. https://doi.org/10.1364/oe.24.014857

[32] Apeksimov, D.V., Geints, Y.E., Zemlyanov, A.A., Kabanov, A.M., Oshlakov, V.K., Petrov, A.V., *et al.* (2018) Controlling Tw-Laser Pulse Long-Range Filamentation in Air by a Deformable Mirror. *Applied Optics*, **57**, 9760-9769. https://doi.org/10.1364/ao.57.009760

[33] Hill, L., Oppo, G., Woodley, M.T.M. and Del'Haye, P. (2020) Effects of Self- and Cross-Phase Modulation on the Spontaneous Symmetry Breaking of Light in Ring Resonators. *Physical Review A*, **101**, Article ID: 013823. https://doi.org/10.1103/physreva.101.013823

[34] Tzallas, P., Charalambidis, D., Papadogiannis, N.A., Witte, K. and Tsakiris, G.D. (2005) Second-Order Autocorrelation Measurements of Attosecond XUV Pulse Trains. *Journal of Modern Optics*, **52**, 321-338. https://doi.org/10.1080/09500340412331301533

[35] Kim, K.Y., Taylor, A.J., Glownia, J.H. and Rodriguez, G. (2008) Coherent Control of Terahertz Supercontinuum Generation in Ultrafast Laser-Gas Interactions. *Nature Photonics*, **2**, 605-609. https://doi.org/10.1038/nphoton.2008.153

[36] Kasparian, J., Ackermann, R., André, Y., Méchain, G., Méjean, G., Prade, B., *et al.* (2008) Electric Events Synchronized with Laser Filaments in Thunderclouds. *Optics Express*, **16**, 5757-5763. https://doi.org/10.1364/oe.16.005757

[37] Rairoux, P., Schillinger, H., Niedermeier, S., Rodriguez, M., Ronneberger, F., Sauerbrey, R., *et al.* (2000) Remote Sensing of the Atmosphere Using Ultrashort Laser Pulses. *Applied Physics B: Lasers and Optics*, **71**, 573-580. https://doi.org/10.1007/s003400000375

[38] D'Amico, C., Houard, A., Franco, M., Prade, B., Mysyrowicz, A., Couairon, A., *et al.* (2007) Conical Forward THz Emission from Femtosecond-Laser-Beam Filamentation in Air. *Physical Review Letters*, **98**, Article ID: 235002. https://doi.org/10.1103/physrevlett.98.235002

[39] Zhao, Y., Witt, T.E. and Gordon, R.J. (2009) Efficient Energy Transfer between Laser Beams by Stimulated Raman Scattering. *Physical Review Letters*, **103**, Article ID: 173903. https://doi.org/10.1103/physrevlett.103.173903

[40] Durand, M., Liu, Y., Forestier, B., Houard, A. and Mysyrowicz, A. (2011) Experimental Observation of a Traveling Plasma Grating Formed by Two Crossing Filaments in Gases. *Applied Physics Letters*, **98**, Article ID: 121110. https://doi.org/10.1063/1.3568888

[41] Mahdy, A.I. (2020) Electric Field Effect on the Relaxation of a Plasma Grating Induced by Two Femtosecond Lasers in Air. *Plasma Research Express*, **2**, Article ID: 025010. https://doi.org/10.1088/2516-1067/ab906c

[42] Liu, Y., Durand, M., Chen, S., Houard, A., Prade, B., Forestier, B., *et al.* (2010) Energy Exchange between Femtosecond Laser Filaments in Air. *Physical Review Letters*, **105**, Article ID: 055003. https://doi.org/10.1103/physrevlett.105.055003

[43] Schulze, C., Roux, F.S., Dudley, A., Rop, R., Duparré, M. and Forbes, A. (2015) Accelerated Rotation with Orbital Angular Momentum Modes. *Physical Review A*, **91**, Article ID: 043821. https://doi.org/10.1103/physreva.91.043821

[44] Andrews, D.L. (2008) Structured Light and Its Applications" An Introduction to Phase-Structured Beams and Nanoscale Optical Forces. Elsevier.

[45] Hu, Z.J., Tan, P.S., Zhu, S.W. and Yuan, X. (2010) Structured Light for Focusing Surface Plasmon Polaritons. *Optics Express*, **18**, 10864-10870. https://doi.org/10.1364/oe.18.010864

[46] Jesacher, A., Fürhapter, S., Bernet, S. and Ritsch-Marte, M. (2004) Size Selective Trapping with Optical "Cogwheel" Tweezers. *Optics Express*, **12**, 4129-4135. https://doi.org/10.1364/opex.12.004129

[47] Sabatyan, A. and Rafighdoost, J. (2017) Azimuthal Phase-Shifted Zone Plates to Produce Petal-Like Beams and Ring Lattice Structures. *Journal of the Optical Society of America B*, **34**, 919-923. https://doi.org/10.1364/josab.34.000919

[48] Islam, M.N., Simpson, J.R., Shang, H.T., Mollenauer, L.F. and Stolen, R.H. (1987) Cross-Phase Modulation in Optical Fibers. *Optics Letters*, **12**, 625-627. https://doi.org/10.1364/ol.12.000625

[49] Teague, M.R. (1982) Irradiance Moments: Their Propagation and Use for Unique Retrieval of Phase. *Journal of the Optical Society of America*, **72**, 1199-1209. https://doi.org/10.1364/josa.72.001199